Pallanca, C, Ferraro, FR, Lanzoni, B, Crociati, C, Saracino, S, Dalessandro, E, Origlia, L, Rich, MR, Valenti, E, Geisler, D, Mauro, F, Villanova, S, Moni Bidin, C and Beccari, G

High-resolution Extinction Map in the Direction of the Strongly Obscured Bulge Fossil Fragment Liller 1*

1

Draft version June 7, 2021
Typeset using LaTeX default style in AASTeX62

High-resolution extinction map in the direction of the strongly obscured bulge fossil fragment Liller 1

Cristina Pallanca,[1,2] Francesco R. Ferraro,[1,2] Barbara Lanzoni,[1,2] Chiara crociati,[1,2] Sara Saracino,[3] Emanuele Dalessandro,[2] Livia Origlia,[2] Michael R. Rich,[4] Elena Valenti,[5,6] Douglas Geisler,[7,8,9] Francesco Mauro,[10] Sandro Villanova,[7] Christian Moni Bidin,[10] and Giacomo Beccari[5]

[1]*Dipartimento di Fisica e Astronomia, Università di Bologna, Via Gobetti 93/2, Bologna I-40129, Italy*
[2]*Istituto Nazionale di Astrofisica (INAF), Osservatorio di Astrofisica e Scienza dello Spazio di Bologna, Via Gobetti 93/3, Bologna I-40129, Italy*
[3] *Astrophysics Research Institute, Liverpool John Moores University, 146 Brownlow Hill, Liverpool L3 5RF, UK*
[4]*Department of Physics and Astronomy, UCLA, PAB 430 Portola Plaza, box 951547, LA CA 90095-1547, USA*
[5]*European Southern Observatory, Karl-Schwarzschild-Straße 2, D-85748 Garching bei München, Germany*
[6]*Excellence Cluster ORIGINS, Boltzmann-Straße 2, D-85748 Garching bei München, Germany*
[7]*Departamento de Astronomía, Universidad de Concepción, Casilla 160 C, Concepción, Chile*
[8]*Instituto de Investigación Multidisciplinario en Ciencia y Tecnología, Universidad de LaSerena. Avenida Raúl Bitrán S/N, La Serena, Chile*
[9]*Departamento de Física y Astronomía, Facultad de Ciencias, Universidad de La Serena. Av.Juan Cisternas 1200, La Serena, Chile*
[10]*Instituto de Astronomía, Universidad Católica del Norte, Av. Angamos 0610, Antofagasta, Chile*

ABSTRACT

We used optical images acquired with the Wide Field Camera of the Advanced Camera for Surveys onboard the *Hubble Space Telescope* and near-infrared data from GeMS/GSAOI to construct a high-resolution extinction map in the direction of the bulge stellar system Liller 1. In spite of its appearance of a globular cluster, Liller 1 has been recently found to harbor two stellar populations with remarkably different ages, and it is the second complex stellar system with similar properties (after Terzan5) discovered in the bulge, thus defining a new class of objects: the Bulge Fossil Fragments. Because of its location in the inner bulge of the Milky Way, very close to the Galactic plane, Liller 1 is strongly affected by large and variable extinction. The simultaneous study of both the optical and the near-infrared color-magnitude diagrams revealed that the extinction coefficient R_V in the direction of Liller 1 has a much smaller value than commonly assumed for diffuse interstellar medium ($R_V = 2.5$, instead of 3.1), in agreement with previous findings along different light paths to the Galactic bulge. The derived differential reddening map has a spatial resolution ranging from $1''$ to $3''$ over a field of view of about $90'' \times 90''$. We found that the absorption clouds show patchy sub-structures with extinction variations as large as $\delta E(B-V) \sim 0.9$ mag.

Keywords: Globular Clusters: individual (Liller1); Milky Way Galaxy; Galactic bulge; Techniques: photometric; HST photometry; Interstellar reddening; Interstellar extinction; Astrophysics - Solar and Stellar Astrophysics

1. INTRODUCTION

Liller 1 is a stellar system historically cataloged as a globular cluster (GC) located in the innermost region of the Galaxy (at only 0.8 kpc from the Milky Way center). It lies very close to the Galactic plane ($l = 354.84, b = -0.16$; Harris 1996), in a region that is affected by large and spatially variable foreground extinction. This is the main reason

[1] Based on observations collected with the NASA/ESA HST (Prop. GO 15231), obtained at the Space Telescope Science Institute, which is operated by AURA, Inc., under NASA contract NAS5-26555. Based on observations (Prop. GS-2013-Q-23) obtained at the Gemini Observatory, which is operated by the Association of Universities for Research in Astronomy, Inc., under a cooperative agreement with the NSF on behalf of the Gemini partnership: the National Science Foundation (United States), the National Research Council (Canada), Agencia Nacional de Investigación y Desarrollo (Chile), the Australian Research Council (Australia), Ministério da Ciência, Tecnologia e Inovação (Brazil), and Ministerio de Ciencia, Tecnología e Innovación Productiva (Argentina). Based on observations gathered with the ESO-VISTA telescope (program ID 179.B-2002).

Corresponding author: Cristina Pallanca
cristina.pallanca3@unibo.it

hindering detailed photometric investigations of its stellar population. One of the first works about the extinction toward Liller 1 dates back to the eighties, when Armandroff & Zinn (1988) estimated a color excess $E(B-V) = 2.7$. Then, Frogel et al. (1995) found $E(J-K) = 1.7$, corresponding to extinction coefficients $A_K = 0.87$, $A_V = 9.5$ and $E(B-V) = 3.0$. In the same work the authors analyzed an offset field and found a larger extinction coefficient, thus suggesting the presence of differential reddening. Later works, both in the optical (Ortolani et al. 1996) and mainly in the near-infrared (NIR; Ortolani et al. 2001; Barbuy et al. 1998; Davidge 2000; Valenti et al. 2010), found values of $E(B-V)$ ranging from 3 up to 3.13, and also highlighted the presence of differential absorption along the line of sight. Gonzalez et al. (2011, 2012) used data from the VISTA Variables in the Vía Láctea (VVV) Survey (Minniti et al. 2010) and derived the mean $(J-K)$ color of red clump giants in 1835 sub-fields in the bulge region (also including the area covered by Liller 1); then, through the comparison with the color of similar stars in the Baade's window, they derived a reddening map with a maximum resolution of $2'$. According to the online simulator[1] based on this work, a color excess $E(J-K) = 1.42 \pm 0.16$, corresponding to $E(B-V) = 2.70$ is found in the direction of Liller 1. More recently, by using the multi-conjugate adaptive-optics system GSAOI at the GEMINI South Telescope, Saracino et al. (2015) obtained the first insight into the cluster population down to its main sequence (MS) turnoff level. They built a reddening map of the central region of Liller 1 with a a spatial resolution of $18'' \times 18''$, finding a mean color excess $E(B-V) = 3.3 \pm 0.2$ and a maximum variation $\delta E(B-V) = 0.34$ within the surveyed field of view (FOV). The dataset was also used to accurately determine the structural and physical parameters (scale radii, concentration parameter, central mass density and total mass) of Liller 1, confirming that this is a massive stellar system (of 1-2 $\times 10^6 M_\odot$) with a very large collision rate (the second-highest after Terzan 5).

Recently, our group performed the very first *Hubble Space Telescope* (HST) observations of Liller 1 in the optical band, securing a set of deep Advanced Camera for Surveys (ACS) images of its central region. By combining these data with the GEMINI NIR observations, Ferraro et al. (2021, hereafter F21) discovered the presence of two distinct stellar sub-populations with remarkably different ages: one as old as ~ 12 Gyr, thus named "Old Population (OP)", and another one much younger, with an age down to only 1 Gyr, that we thus call "young population (YP)". This discovery unquestionably demonstrates that Liller 1 is not a genuine GC. It is the second stellar system in the bulge (after Terzan 5; Ferraro et al. 2009) that appears as a GC, but harbors, instead, a young sub-population of stars. The oldest populations in Liller 1 and in Terzan 5 are impressively similar, in agreement with the typical age of bulge GCs, thus indicating that these systems formed at the same cosmic epoch, from gas clouds with comparable chemistry. In turn, the chemical abundance patterns measured in Terzan 5 are remarkably similar to those observed in the bulge field stars (Ferraro et al. 2016a; Lanzoni et al. 2010; Origlia et al. 2011, 2013, 2019; Massari et al. 2015). These observational facts allowed F21 to define a new class of stellar systems, the "Bulge Fossil Fragments (BFFs)": these are stellar aggregates with the appearence of massive GCs orbiting the Galactic bulge, formed at the epoch of the Galaxy assembling, and harbouring in addition to the old population, a younger (1-3 Gyr old) component. These stellar systems could, in fact, be interpreted as the surviving relics of much more massive primordial structures that generated the Galactic bulge (similar to the giant clumps observed in the star forming regions of high-redshift galaxies; Immeli et al. 2004; Carollo et al. 2007; Elmegreen et al. 2008; Genzel et al. 2011; Tacchella et al. 2015; Behrendt et al. 2016).

Within this exciting scenario, we are now coordinating a project aimed at reconstructing the origin and the star formation history of the latest discovered BFF. Thus, while future specific papers will be devoted to reconstruct the star formation history of Liller 1 (Emanuele Dalessandro et al., in preparation) and the chemical abundance patterns of its sub-populations (Livia Origlia et al., in preparation), here we determine the first high resolution differential reddening map in the direction of the system. This map was used by F21 to construct the de-reddened color-magnitude diagram (CMD) that revealed the presence of the young population in Liller 1 and to study its properties. The paper is organized as follows. In Section 2 we describe the dataset used in this work and the main steps of the photometric analysis. In Section 3 we present the determination of the differential reddening map of Liller 1. In Section 4 we discuss the main results of the paper and summarize the conclusions.

2. OBSERVATIONS AND DATA ANALYSIS

2.1. *Datasets*

[1] *http://mill.astro.puc.cl/BEAM/calculator.php*

Table 1. Summary of the used datasets

Instrument	Program ID	PI	Date [yyyy/mm/dd]	Filter	$N_{exp} \times t_{exp}$
HST/ACS-WFC	GO 15231	Ferraro	2019/08/17	F606W	$2 \times 1361s$, $2 \times 1360s$, $2 \times 1260s$
				F814W	$2 \times 855s$, $1 \times 854s$, $1 \times 837s$, $2 \times 836s$

The photometric dataset used for this work consists in a combination of observations obtained at optical and NIR wavelengths. By using the Wide Field Channel (WFC) of the ACS on board the HST, we secured the first set of high-resolution optical images ever acquired for Liller 1 (GO 15231, PI: Ferraro). The observations have been performed in the filters F606W (V) and F814W (I), and they consist in a set of 6 deep images per filter (see Table 1). To study Liller 1 at NIR wavelengths we used a dataset of high-resolution J and Ks (hereafter K) images acquired with the multiconjugate adaptive-optics assisted camera GeMS/GSAOI at the GEMINI South Telescope (GS-2-13-Q-23, PI: Geisler). These images were already used to obtain a first insight into the stellar population in Liller1 by Saracino et al. (2015). All the images are dithered by few pixels, in order to avoid spurious effects due to bad pixels. In addition, the NIR datasets were secured following a dither pattern large enough to fill the inter-chip gaps, thus allowing a complete coverage of the innermost $\sim 100'' \times 100''$ region of the system.

2.2. *Photometric analysis, astrometry and magnitude calibration*

The data reduction of the ACS-WFC images has been performed on the CTE-corrected (`flc`) images after a correction for Pixel-Area-Map. The photometric analysis was performed via the point-spread function (PSF) fitting method, by using DAOPHOT (Stetson 1987) and following the "standard" approach used in previous works (e.g., Pallanca et al. 2017; Dalessandro et al. 2018; Cadelano et al. 2019). Spatially variable PSF models were derived for each image by using some dozens of bright and nearly isolated stars. The PSF was modelled adopting an analytical `MOFFAT` function plus a spatially variable look-up table and it has been applied to all the identified sources with flux peaks at least 3 σ above the local background. We then built a master-list containing all the stellar-like sources detected in more than 3 images in at least one filter. In order to improve the level of completeness, we performed an accurate inspection of the residual images, in order to search for additional stellar sources missed during the first iteration of the analysis because of the serious crowding conditions. This procedure allowed us to recover a few dozens of stars, which were added to the master-list.

We then forced a fit at the position of each star belonging to the master-list, in each frame, by using the `ALLFRAME` package (Stetson 1987, 1994). For each star, multiple magnitude estimates from different exposures were homogenised by using DAOMATCH and DAOMASTER, and their weighted mean and standard deviation were finally adopted as the star magnitude and photometric error. The final optical HST instrumental catalog contains all the stars measured in at least 3 images in any of the two filters. For each star, it lists the instrumental coordinates, the mean magnitude in each filter and two quality parameters (*chi* and *sharpness*).[2]

The instrumental optical magnitudes were calibrated onto the VEGAMAG photometric system by using the updated recipes and zero-points available in the HST web-sites. The instrumental coordinates were first corrected for geometric distortion and then reported to the absolute coordinate system (α, δ) defined by the World Coordinate System by using stars in common with the publicly available Gaia DR2 catalog (Gaia Collaboration et al. 2016a,b). Although only disk field stars have been found in common with the Gaia catalog (due to the very high extinction toward this stellar system), the resulting 1σ astrometric accuracy is $\sim 0.1''$. The reduction of the ACS-WFC images has been limited to chip 1 because of the negligible overlap between chip 2 and the FOV covered by the GeMS observations (see Figure 1).

At this point, the sample of stars detected in the optical and in the NIR catalogs were compared. From a first analysis it was evident that each catalog contained some objects missed in the other, mainly due to the faintness of the source and/or its vicinity to very bright objects with extreme (blue or red) colors. On the other hand, the analysis also demonstrated that, because of the large extinction in the direction of the system, the V-band exposures are significantly shallower that those secured through the I filter, and, similarly, the J images are much less deep

[2] The *chi* parameter is the ratio between the observed and the expected pixel-to-pixel scatter between the model and the profile image. The *sharpness* parameter quantifies how much the source is spatially different from the PSF model. In particular, positive values are typical of more extended sources, such as galaxies and blends, while negative values are expected in the case of cosmic rays and bad pixels.

than those obtained through the K filter. This clearly indicated that the optimal solution for the accurate study of the stellar populations in Liller 1 including optical and NIR filters consisted in combining the I and the K images. We thus proceeded with a second-level analysis starting from the independent reduction of the optical dataset and the 6 best-quality (per each filter) NIR images. Two lists of sources have been obtained: one comprising all the stars detected in the I filter and one including the objects identified in the K band. The I-band list contained all the stars measured in at least 3 frames, over the 6 available. The K-band list contained all the stars measured in at least 3 over the 6 images analysed. We thus combined the two datasets, building a single master-list that contains all the detected stars (some having magnitude measured in both filters, others having only the I or the K measure). The sources detected only in the I images were then searched and analysed also in the K images, and vice versa, thus maximizing the information provided by the two filters separately. The final magnitudes of this combined analysis were homogenized to the calibrated stand-alone HST and GeMS catalogs, in the Vegamag and 2MASS systems, respectively. The magnitudes of the brightest stars ($K < 12.5$), which are saturated in the Gemini observations, have been recovered (up to $K \sim 10$) from the PSF photometry of VVV Survey data performed by Mauro et al. (2013). The final catalog reports the I and K band magnitudes (together with the V and J ones, if measured) for 43629 stars detected in both HST and GeMS images.

Figure 1 shows the FOV sampled by chip1 of the HST/ACS-WFC (outlined in yellow) and by the GeMs observations (dashed blue line). As apparent, the overlapping region, from which we can construct the $(I, I-K)$ CMD and determine the differential reddening map, corresponds to an area of about $\sim 90'' \times 90''$ (green area), almost centered onto the gravity center (i.e. determined as the photometric barycenter) of Liller 1 (Saracino et al. 2015). Hereafter, all the discussion and plots are made considering only the stars in this region. Their CMD distribution is shown in three different color and magnitude combinations in Figure 2: from left, to right, the optical $(I, V-I)$ CMD, the "hybrid" $(I, I-K)$ CMD, and the NIR $(K, J-K)$ one. As expected, extinction along the line of sight limits the deepness of the sample expecially in the optical diagram. The differential effect of the reddening is particularly visible in the deformed morphology of the red clump, which appears to be largely stretched along the direction of the reddening vector (from top-left, to bottom-right), especially in the optical and hybrid CMDs. This clearly shows that any meaningful analysis of the stellar populations of Liller 1 requires an appropriate modelling of and correction for the differential reddening effects.

For almost all the stars in the catalog, we also measured the relative proper motions by exploiting the time base-line of 6.3 yr separating the available observations. This allowed us to distinguish the stars belonging to Liller 1, from Galactic field interlopers (respectively, black and orange dots in Figure 2). The procedure used for the proper motion measurement and the adopted selection criteria for membership have been presented in F21.

3. DIFFERENTIAL REDDENING MAP

3.1. *Reddening laws*

As is well known, interstellar reddening is due to the absorption and scattering of the radiation caused by dust clouds along the light path to the observer. This phenomenon makes the flux of a given source systematically fainter and the color systematically redder than their true (emitted) values, with an efficiency that strongly depends on the wavelength (increasing at shorter wavelengths). The entity of reddening is usually parametrised by the color excess $\mathrm{E}(B-V)$, defined as the difference between the observed color $(B-V)$ and the intrinsic color $(B-V)_0$ that, for stars, is mainly fixed by the temperature of the source.

The extinction law, i.e., the dependence of the absorption coefficient on wavelength (A_λ) can be expressed as (see also the formulations by Cardelli et al. 1989; O'Donnell 1994; Fitzpatrick & Massa 1990; Fitzpatrick 1999):

$$\mathrm{A}_\lambda = \mathrm{R}_V \times c_{\lambda,\mathrm{R}_V} \times \mathrm{E}(B-V), \tag{1}$$

where $c_{\lambda,\mathrm{R}_V} = 1$ is commonly adopted at the V-band wavelength ($c_{V,\mathrm{R}_V} = 1$). The parameter R_V is usually set equal to 3.1, which is the standard value for diffuse interstellar medium (Schultz & Wiemer 1975; Sneden et al. 1978). This is indeed the value assumed in all previous works devoted to the estimate of reddening in the direction of Liller 1 (see the Introduction). Particular attention, however, has to be given to the extinction toward the inner Galaxy (Popowski 2000; Nataf et al. 2013; Alonso-García et al. 2017; Casagrande & VandenBerg 2014; Pallanca et al. 2021, and references therein), where the R_V value seems to vary along different directions. For example Nataf et al. (2013) suggested that $\mathrm{R}_V = 2.5$ is more appropriate to reproduce the bulge populations, while some other authors quote larger values (e.g., $\mathrm{R}_V = 3.2$; Bica et al. 2016; Kerber et al. 2019).

Decreasing the value of R_V makes the parameter c_{λ,R_V} (thus, the extinction law A_λ/A_V) more steeply dependent on wavelength. This is illustrated in the upper panel of Figure 3, where the two curves refer to the canonical R_V value ($R_V = 3.1$, blue line) and to $R_V = 2.5$ (red line). As shown in the central panel of the figure, the difference between $c_{\lambda,2.5}$ and $c_{\lambda,3.1}$ is quite small in the photometric bands considered in this work (marked by the dashed vertical lines). However, this difference increases by one order of magnitude when these coefficients are multiplied by their respective value of R_V: this is shown in the bottom panel of the figure, plotting $R_{\lambda,R_V} \equiv R_V \times c_{\lambda,R_V}$. In turn, recalling that $E(B-V) = A_\lambda/R_{\lambda,R_V}$, this implies that any given value of the absorption coefficient A_λ corresponds to a significantly different color excess $E(B-V)$ if $R_V = 2.5$ is assumed in place of the standard value $R_V = 3.1$. Hence, the value of $E(B-V)$ and the distance modulus (μ_0) necessary to superpose an isochrone onto an observed CMD change if $R_V = 2.5$ is adopted instead of $R_V = 3.1$. The bottom panel of Figure 3 also shows that the difference between $R_{\lambda,2.5}$ and $R_{\lambda,3.1}$ is not constant, but significantly increases (in absolute value) for decreasing wavelength in the range relevant for the present study: it varies between ~ 0.1 at $\lambda \simeq 21326.7$ Å (the K band) and ~ 0.6 at $\lambda \simeq 5810.8$ Å (the effective wavelength of the F606W filter; Rodrigo et al. 2012; Rodrigo & Solano 2020).[3] In turn, the increasing difference between $R_{\lambda,2.5}$ and $R_{\lambda,3.1}$ for decreasing wavelength necessarily implies that two isochrones, the one shifted to the observed plane by adopting $R_V = 3.1$, the other shifted under the assumption of $R_V = 2.5$, cannot simultaneously reproduce the NIR and the optical CMDs of a stellar system. This is illustrated in Figure 4, where the optical $(I, V-I)$, hybrid $(I, I-K)$ and NIR $(K, J-K)$ CMDs of Liller 1 are shown together with an isochrone (Marigo et al. 2017) computed for an age $t = 12$ Gyr and a global metallicity [M/H]$= -0.3$. The black dashed line shows the location in the three CMDs of the isochrone obtained by assuming $R_V = 3.1$, $E(B-V) = 3.30$ and $\mu_0 = 14.55$, which are the values needed to make it reproduce the observed NIR CMD (Saracino et al. 2015). However, no reasonable match of the observations can be simulatenously obtained in the optical and hybrid CMDs. Conversely, by adopting $R_V = 2.5$ (red line) all the evolutionary sequences of the cluster in any wavelength combination are well reproduced. This demonstrates that the canonical reddening law is not appropriate in that direction of the sky, and a much lower value of R_V is needed toward Liller 1, in agreement with what suggested in the pioneering work of (Frogel et al. 1995) and what previously found for other bulge directions (e.g., Popowski 2000; Nataf et al. 2013; Alonso-García et al. 2017; Casagrande & VandenBerg 2014; Saha et al. 2019; Pallanca et al. 2021).

The manifest inadequacy of $R_V = 3.1$ in the direction of Liller 1 came not into light in previous works because they were all based on NIR or optical datasets separately: it is indeed the simultaneous analysis of these CMDs that finally revealed the necessity of a much lower value of R_V. Of course, however, a proper comparison between theoretical isochrones and observations first requires to correct the CMDs for the effects of differential reddening, which is responsible for the distortions of the evolutionary sequences clearly visible in Figure 4.

Our result (i.e., R_V=2.5) is perfectly in agreement with previous works aimed to estimate the reddening law in the Bulge direction (Nataf et al. 2013; Saha et al. 2019). For example, R_V=2.5 perfectly corresponds to the peak of the distribution shown in Figure 8 of Nataf et al. (2013): indeed, as explicitly discussed in the conclusions of that paper, the mean value of the distribution, $A_I/E(V-I) \sim 1.217$, corresponds to R_V=2.5. On the other hand, we found that the absorption coefficients derived by Saha et al. (2019) in the direction of the Baade's window and shown as black circles in their Figure 8 are well reproduced by the O'Donnell (1994) extinction law calculated for $R_V \sim 2.0$, and the values obtained for R_V=2.5 place in the middle between these points and those corresponding to the standard R_V=3.1 (red circles in their figure). Note that a value as small as R_V=2.0, even if surprising, is still in agreement with the left-hand tail of the distribution shown in Figure 8 of Nataf et al. (2013). Hence, our result is perfectly in agreement with previous works and it brings further evidence that the commonly adopted R_V=3.1 is likely inappropriate toward the Bulge, while a precise estimate of the extinction law in each specific direction is required (see also Pallanca et al. 2021).

3.2. *The differential reddening map of Liller 1*

The interstellar extinction along the Galactic plane and in the direction of the Galactic center can be highly spatially variable (differential reddening), on scales that can be as small as a few arcseconds. Since this spatial dimension is significantly smaller than the apparent size of most Galactic stellar systems, the CMD of star clusters affected by differential reddening shows a systematic elongation of all the evolutionary sequences along the direction of the

[3] Following the prescriptions of Cardelli et al. (1989) and O'Donnell (1994), we find that, if $R_V = 3.1$, the corresponding values in the four photometric bands here considered are: $R_{606} = 2.89$, $R_{814} = 1.90$, $R_J = 0.89$, and $R_K = 0.37$. If $R_V = 2.5$, then: $R_{606} = 2.30$, $R_{814} = 1.43$, $R_J = 0.64$, and $R_K = 0.27$.

reddening vector. In turn, this prevents the accurate characterization of their photometric properties, with a non negligible impact on the determination of fundamental parameters such as, for instance, the distance and age (e.g., Bonatto et al. 2013). To model and correct for the effect of differential reddening in GCs, two main approaches have been adopted in the literature. Schematically: (1) the "cell by cell" method, which consists in dividing the observed FOV in a number of cells, build the CMD of the stars included in each cell, and calculate the reddening value in each cell from the color and magnitude displacements with respect to the bluest CMD (Heitsch & Richtler 1999; Piotto et al. 1999; von Braun & Mateo 2001; McWilliam & Zoccali 2010; Nataf et al. 2010; Gonzalez et al. 2011, 2012; Massari et al. 2012; Bonatto et al. 2013; Saracino et al. 2015), and (2) the "star by star" approach, which consists in estimating the reddening of each star in the catalog from the relative displacement between its "local CMD", i.e., the CMD built with the spatially closest objects, and the cluster mean ridge line (Milone et al. 2012; Bellini et al. 2013; Saracino et al. 2019; Pallanca et al. 2019; Cadelano et al. 2020). In the cited papers, different authors used stars in different evolutionary sequences as reference for the determination of the color and magnitude displacements: MS, horizontal branch, red giant branch (RGB) stars, and even variable RR Lyrae (Alonso-García et al. 2011, and references therein). In all cases, the spatial resolution is driven by the need for a statistically reliable sample of stars to build the cell or local CMDs. To determine the differential extinction map in the direction of Liller 1 we used the "star by star" method, adopting the RGB, sub-giant branch (SGB) and bright MS stars as reference, as already tested in a previous work (Pallanca et al. 2019). In addition, because of the results discussed in the previous section, we adopted $R_V = 2.5$.

The first step consists in the definition of the reference mean ridge line (MRL) of the OP of Liller 1. This has been determined in the proper motion cleaned, hybrid $(I, I-K)$ CMD, which is significantly deeper than any other available color-combination (even more than the $(K, J-K)$ CMD which is likewise deep but with a worst signal to noise ratio in the J filter at the bottom of the MS; see Figure 2), thus allowing us to also use stars along the SGB and MS phases. In turn, this implies a significant increase of the spatial resolution of the output reddening map, with respect to the case where only RGB stars could be used. In order to remove poorly measured objects that can bias the procedure, we first considered only stars with high-quality photometry, by adopting 3-σ cuts in the *chi* and *sharpness* parameter distributions. The considered sample, comprising the RGB, SGB and the upper MS of the OP, was divided in magnitude bins of variable size (ranging from 0.25 to 1 mag), in order to best sample the morphological changes of the sequence in the MS turnoff region. The mean color of each considered bin was then determined after a 3σ-clipping rejection, in order to remove any residual interlopers.

Once the MRL is defined, we considered all the stars in the catalog (i.e., not only the high-quality objects) and for each of them we selected, from the high-quality pool (and proper motion selected) sample, the N_* sources spatially lying in the vicinity of the star under investigation. The method consists in determining the value of $\delta E(B-V)$ required to shift the MRL of the system along the direction of the reddening vector until it fits the local CMD defined by these N_* nearby sources. Of course, the larger is the number of sources (N_*), the better defined is the local CMD. However, to keep the spatial resolution as high as possible, we constrained N_* below a maximum value and we assumed a limiting radial distance ($r_{\rm lim}$) within which the nearby sources can be selected. We set $N_{*,\rm max} = 30$ and $r_{\rm lim} = 3''$. As soon as one of these two conditions is satisfied, the other one is no longer considered. Since the stellar density is higher in the center and decreases with radius, this approach naturally yields an "adaptive grid" producing reddening maps with higher (lower) spatial resolution in the central (external) regions.

As described in F21, the sub-sample with measured PM represents about 80% of the entire sample. In particular due to dithering patterns adopted in the GeMS/GSAOI observations (aimed at covering the inter-chip gaps), a sort of external corona and a central cross of the FOV was not properly sampled by all the considered NIR exposures to allow accurate PM measures. Thus, the procedure aimed at the construction of the reddening map has been applied twice. The first time, only stars classified as Liller 1 members from their measured proper motion were included in the high-quality pool. The second time, in order to cover the entire FOV, no proper motion selection was used. The differential reddening estimates obtained from these two approaches are fully compatible (as already found for NGC 6440 in Pallanca et al. 2019), demonstrating that the potential presence of a few field interlopers does not affect the result. Hence, the final differential reddening value assigned to each star has been obtained, whenever possible, from the (formally more rigorous) proper motion based method, and complemented with the value derived neglecting the proper motion selection in the other cases.

Because of the large central densities, the number of stars within a circle of $3''$ radius is typically much larger than 30 in the inner cluster regions; hence the $N_{*,\rm max}$ closest sources are typically selected within a distance much smaller than $r_{\rm lim}$ from each star under investigation in this region. The opposite is true in the outskirts, where the driving

parameter for the selection of nearby sources becomes $r_{\rm lim}$. This is clearly visible in the left panel of Figure 5: the distance used for the selection of the nearby stars defining the local CMD can be as small as $1''$ in the central regions, while it increases up to the maximum value ($r_{\rm lim} = 3''$) close to the boundaries of the analysed FOV, where only semicircles toward the center can be drawn. The few spots visibile on the map correspond to local increases of the selection radius due to the presence of saturated stars. The discontinuities in the innermost spot and at the outermost edge of the FOV are due to the transition between reddening estimates that take into account/neglect the proper motion condition (which is unavailable in these regions: by keeping larger numbers of stars, this allows us to use a slightly smaller selection radius).

The comparison between the MRL of the cluster OP and the local CMDs has been performed in the magnitude range $19.5 < I < 26$, in order to discard potentially saturated and too faint (hence not well measured) objects. We also performed a 3σ rejection in order to exclude from the analysis all the stars with a color distance from the MRL significantly larger than that of the bulk of the selected objects. This is useful to exclude field interlopers not removed by the proper motion analysis and/or discard non canonical stars with intrinsic colors different from those of the cluster main populations (Pallanca et al. 2010, 2013, 2014; Cadelano et al. 2015a; Dalessandro et al. 2014; Ferraro et al. 2015, 2016b, 2018).

The comparison was performed by shifting the MRL along the reddening direction (which is fixed by the adopted extinction law) in steps of $\delta{\rm E}(B-V)$. For each considered step, we calculated the residual color ΔIK as:

$$\Delta IK = \sum_{i=1}^{N_*} \left(|IK_{{\rm obs},i} - IK_{{\rm MRL},i}| + w_i \cdot |IK_{{\rm obs},i} - IK_{{\rm MRL},i}| \right), \tag{2}$$

where $IK_{{\rm obs},i}$ is the $(I-K)$ color observed for each of the N_* selected objects constituting the local CMD, $IK_{{\rm MRL},i}$ is that of the MRL at the same level of magnitude, and the weight w_i takes into account both the photometric error on the color (σ) and the spatial distance (d) of the i^{th} source from the star under investigation, according to the following expression:

$$w_i = \frac{1}{d_i \cdot \sigma_i} \left[\sum_{j=1}^{N_*} \left(\frac{1}{d_j \cdot \sigma_j} \right) \right]^{-1}. \tag{3}$$

The second term is meant to give more weight to the closest stars, thus increasing the accuracy of the local reddening estimate, reducing the impact of using large selection distances where the level of dust absorption could change. Note that we cannot reduce equation (2) to the second term only, because a bright object (with small photometric errors) close to the central star would dominate the weight and make the reddening estimate essentially equal to the value needed to move the MRL exactly on that object. The final differential reddening value assigned to each star is the value of the step $\delta{\rm E}(B-V)$ that minimises the normalised residual color ($\Delta IK/N_*$). The spatial distribution of differential extinction values thus derived for each star constitutes the differential reddening map shown in the right panel of Figure 5.

We emphasize that in the adopted procedure, the value of $\delta{\rm E}(B-V)$ assigned to each star is not guided by its position in the CMD with respect to the cluster MRL, but by the position of its N_* neighboring stars (i.e., the N_* stars spatially adjacent on the plane of the sky to the object under analysis). This ensures that we are correcting for a phenomenon (differential reddening) affecting the region of sky where the star is located, not for possible intrinsic properties of the star itself (e.g., its chemical abundance).

4. DISCUSSION AND CONCLUSIONS

Following the procedure described above, we built the differential reddening map in the direction of Liller 1, over a total FOV of about $90 \times 90''$, and with an angular resolution smaller than $3''$(right panel of Figure 5). It appears patchy on spatial scales of just a few arcsecs, and it presents two main highly-reddened blobs located on the east and north sides of the sampled FOV. The less absorbed region (lighter color in the figure) is located in an almost vertical strip on the west side, flowing into the north-west and south-east corners. Overall, the map graphically demonstrates a large amount of differential reddening, with $\delta{\rm E}(B-V)$ ranging between -0.57 to 0.37. This corresponds to differential absorptions of 2.16, 1.35, 0.60 and 0.25 mag in the V, I, J and K filters, respectively. Note that the maximum variation of ${\rm E}(B-V)$ found here (~ 0.9) is significantly larger than that estimated in Saracino et al. (2015), who quote $\delta E(B-V) = 0.34$. This is however expected both because of the larger ${\rm E}(B-V)$ (for a constant percentage of

variation, the larger is the absolute value, the larger is the variation), and because of the different spatial resolution of the two reddening maps. In fact, the much larger cells ($18'' \times 18''$) in the map of Saracino et al. (2015) have the effect of smoothing local fluctuations, hence decreasing the amplitude of the $E(B-V)$ variations.

The CMDs corrected for absolute differential reddening are shown in Figure 6 and reveal a clear improvement in their overall quality with respect to the observed ones (Figure 2). Indeed, after correction, the evolutionary sequences appear sharper (i.e., thinner and better defined) in all the filter combinations. In particular, the YP is much more evident and much better separated in color with respect to the OP (see also F21). To quantify the effectiveness of the correction, we estimated the width in the $(I-K)$ color at the the level of the faint RGB ($15 < K < 16$) and of the red-clump ($14 < K < 14.7$) before and after the correction: the dispersion in color decreases from ~ 0.2 mag, down to ~ 0.1 mag in both cases. The position in the reddening corrected CMDs of a 12 Gyr old isochrone with [M/H]$= -0.3$, under the assumption of $R_V = 2.5$, a mean absolute color excess $E(B-V) = 4.52 \pm 0.10$ and a distance modulus $\mu_0 = 14.65 \pm 0.15$ (see F21) is marked by the red lines (which are the same as in Figure 4). The very good match of the observations in all the three color combinations clearly confirms that $R_V = 2.5$ is the most appropriate value in the direction of Liller 1, while the assumption of the standard value ($R_V = 3.1$) brings to a severe disagreement in the optical and in the hybrid CMDs (analogously to what is shown in Figure 4). The quoted value of μ_0 is consistent with the latest determination (Saracino et al. 2015), while the average reddening estimated here is significantly larger than previously found (e.g., 3.3 in Saracino et al. 2015). However, the difference is almost entirely ascribable to the different value of R_V adopted here and in previous works, and it becomes significantly smaller in terms of the absorption coefficients: for instance, here we have $A_K = 2.5 \times 0.107 \times 4.52 = 1.21$ and $A_J = 2.5 \times 0.257 \times 4.52 = 2.90$, while Saracino et al. (2015) adopted $A_K = 3.1 \times 0.113 \times 3.3 = 1.16$ and $A_J = 3.1 \times 0.281 \times 3.3 = 2.86$, which are well consistent with our values.

Once the average reddening $E(B-V)$ is known, the absolute reddening map in the direction of Liller 1 can be constructed. This is shown in Figure 7, where different values of the absolute color excess $E(B-V)$ are coded as in the plotted color-bar. We stress again that while the absolute values of $E(B-V)$ depend on the adopted absorption coefficients and extinction law, the main structures distinguishable in the derived map are largely independent of them.

The CMDs shown in Figure 6 are the cleanest and most accurate ever obtained for Liller 1, and they led F21 to the discovery of a 1-3 Gyr old stellar population (the YP) co-existing with the OP in this system. This is illustrated in two complementary ways in Figure 8. The left panel shows a "canonical" CMD, where each dot corresponds to an individual star. It provides a clear distinction of the main evolutionary sequences of the OP, and allows a clean separation of the YP from the RGB of the OP. The right panel, instead, shows the stellar density distribution in the CMD (Hess diagram), with the darker colors being associated to regions of larger numbers of stars per color-magnitude cell. This way immediately allows the identification of the most populated sequences (e.g., the MS), making clearer the transition between the MS and the highly dense SGB of the OP (which are both typical of very old stellar populations), and the much more prominent MS of the YP, extending to brighter magnitudes and bluer colors, as expected for younger stellar populations. The analysis of this CMD and the comparison with different sets of isochrones suggest that the YP is made of stars not only with an age of just 1-3 Gyr, but probably also with a higher metallicity than the OP (see the isochrones plotted in Figure 8 and the discussion in F21). This finding unquestionably demonstrates that Liller 1 is not a GC, but a stellar system with a much more complex star formation history. This is the second case (after Terzan 5; Ferraro et al. 2009, 2016a) of a GC-like system in the Galactic bulge showing these peculiarities. F21 demonstrated that the oldest stellar populations observed in Liller 1 and in Terzan 5 are impressively similar, thus indicating that these systems formed at the same cosmic epoch, from gas clouds with comparable chemistry(Ferraro et al. 2009; Origlia et al. 2011, 2013; Massari et al. 2014). In turn, the striking similarity between the chemical patterns measured in Terzan 5 and those observed in the bulge field stars suggests that these systems possibly are the remnants of massive clumps that contributed to form the bulge at the epoch of the Galaxy assembling. The identification of the BFFs as sites of recent star formation also has a crucial impact on the presence and the origin of young stars in the Galactic bulge field. As shown in this paper the correct evaluation of the reddening map in the direction of these highly obscured stellar systems is a crucial requirement to probe their stellar populations and recontruct their star formation history (Emanuele Dalessandro et al., in preparation).

We thank the anonymous referee for the useful comments that improved the paper. This work is part of the project Cosmic-Lab at the Physics and Astronomy Department of the Bologna University. The research was funded by the Italian MIUR throughout PRIN-2017 grant awarded to the project 2017K7REXT *Light-on-Dark* (PI:Ferraro). We also

thank financial support from the Mainstream project SC3K - Star clusters in the inner 3 kpc (1.05.01.86.21) granted by INAF. This research has made use of the SVO Filter Profile Service (http://svo2.cab.inta-csic.es/theory/fps/) supported from the Spanish MINECO through grant AYA2017-84089. SS gratefully acknowledges financial support from the European Research Council (ERC-CoG-646928, Multi-Pop). D.G. gratefully acknowledges support from the Chilean Centro de Excelencia en Astrofísica y Tecnologías Afines (CATA) BASAL grant AFB-170002. D.G. also acknowledges financial support from the Dirección de Investigación y Desarrollo de la Universidad de La Serena through the Programa de Incentivo a la Investigación de Académicos (PIA-DIDULS).

The photometric data that support the plots and other findings of this study are available from the corresponding author upon reasonable request.

Facilities: HST(ACS-WFC); GeMS/GSAOI.

Software: `Matplotlib` (Hunter 2007); `NumPy` (Harris et al. 2020); `extinction` (Barbary 2016).

REFERENCES

Alonso-García, J., Mateo, M., Sen, B., Banerjee, M., & von Braun, K. 2011, AJ, 141, 146

Alonso-García, J., Minniti, D., Catelan, M., et al. 2017, ApJL, 849, L13. doi:10.3847/2041-8213/aa92c3

Armandroff, T. E. & Zinn, R. 1988, AJ, 96, 92. doi:10.1086/114792

Barbary, K. 2016, Extinction V0.3.0, Zenodo, doi:10.5281/zenodo.804967

Barbuy, B., Bica, E., & Ortolani, S. 1998, A&A, 333, 117

Bellini, A., Piotto, G., Milone, A. P., et al. 2013, ApJ, 765, 32

Behrendt, M., Burkert, A., & Schartmann, M. 2016, ApJL, 819, L2

Bica, E., Ortolani, S., & Barbuy, B. 2016, PASA, 33, e028. doi:10.1017/pasa.2015.47

Bonatto, C., Campos, F., & Kepler, S. O. 2013, MNRAS, 435, 263

Cadelano, M., Pallanca, C., Ferraro, F. R., et al. 2015a, ApJ, 807, 91

Cadelano, M., Ferraro, F. R., Istrate, A. G., et al. 2019, ApJ, 875, 25

Cadelano, M., Saracino, S., Dalessandro, E., et al. 2020, arXiv e-prints, arXiv:2004.06131

Cardelli, J. A., Clayton, G. C., & Mathis, J. S. 1989, ApJ, 345, 245

Carollo, C. M., Scarlata, C., Stiavelli, M., Wyse, R. F. G., & Mayer, L. 2007, ApJ, 658, 960

Casagrande, L. & VandenBerg, D. A. 2014, MNRAS, 444, 392. doi:10.1093/mnras/stu1476

Dalessandro, E., Cadelano, M., Vesperini, E., et al. 2018, ApJ, 859, 15

Dalessandro, E., Pallanca, C., Ferraro, F. R., et al. 2014, ApJL, 784, L29

Davidge, T. J. 2000, ApJS, 126, 105.

Elmegreen, B. G., Bournaud, F. & Elmegreen, D. M. 2008,ApJ, 688, 67.

Ferraro, F. R., Dalessandro, E., Mucciarelli, A., et al. 2009, Nature, 462, 483

Ferraro, F. R., Pallanca, C., Lanzoni, B., et al. 2015, ApJL, 807, L1

Ferraro, F. R., Lapenna, E., Mucciarelli, A., et al. 2016b, ApJ, 816, 70

Ferraro, F. R., Massari, D., Dalessandro, E., et al. 2016a, ApJ, 828, 75

Ferraro, F. R., Lanzoni, B, Raso, S., et al. 2018, ApJ, 860, 36

Ferraro, F. R., Pallanca, C., Lanzoni, B, et al. 2021, Nature Astronomy, 5, 311 (F21)

Fitzpatrick, E. L., & Massa, D. 1990, ApJS, 72, 163

Fitzpatrick, E. L. 1999, PASP, 111, 63

Frogel, J. A., Kuchinski, L. E., & Tiede, G. P. 1995, AJ, 109, 1154

Gaia Collaboration, Brown, A. G. A., Vallenari, A., et al. 2016, A&A, 595, A2

Gaia Collaboration, Prusti, T., de Bruijne, J. H. J., et al. 2016, A&A, 595, A1

Genzel, R., Newman, S., Jones, T., et al. 2011, ApJ, 733, 101

Gonzalez, O. A., Rejkuba, M., Zoccali, M., Valenti, E., & Minniti, D. 2011, A&A, 534, A3

Gonzalez, O. A., Rejkuba, M., Zoccali, M., et al. 2012, A&A, 543, A13

Harris, W. E. 1996, VizieR Online Data Catalog, 7195,

Harris, C. R., Millman, K. J., van der Walt, S. J., et al. 2020, Nature, 585, 357. doi:10.1038/s41586-020-2649-2

Heitsch, F., & Richtler, T. 1999, A&A, 347, 455

Hunter, J. D., 2007, Computing in Science & Engineering, 9, 90

Immeli, A., Samland, M., Gerhard, O. & Westera, P. 2004,A&A, 413, 547

Kerber, L. O., Libralato, M., Souza, S. O., et al. 2019, MNRAS, 484, 5530. doi:10.1093/mnras/stz003

Lanzoni, B., Ferraro, F. R., Dalessandro, E., et al. 2010, ApJ, 717, 653

Marigo, P. et al. 2017, ApJ, 835, 77.

Massari, D., Mucciarelli, A., Dalessandro, E., et al. 2012, ApJL, 755, L32

Massari, D., Mucciarelli, A., Ferraro, F. R., et al. 2014, ApJ, 795, 22. doi:10.1088/0004-637X/795/1/22

Massari, D., Dalessandro, E., Ferraro, F. R., et al. 2015, ApJ, 810, 69

Mauro, F., Moni Bidin, C., Chené, A.-N., et al. 2013, RMxAA, 49, 189

McWilliam, A., & Zoccali, M. 2010, ApJ, 724, 1491

Milone, A. P., Piotto, G., Bedin, L. R., et al. 2012, A&A, 540, A16

Minniti, D., Lucas, P. W., Emerson, J. P., et al. 2010, NewA, 15, 433

Nataf, D. M., Udalski, A., Gould, A., Fouqué, P., & Stanek, K. Z. 2010, ApJL, 721, L28

Nataf, D. M., Gould, A., Fouqué, P., et al. 2013, ApJ, 769, 88

O'Donnell, J. E. 1994, ApJ, 422, 158

Origlia, L., Rich, R. M., Ferraro, F. R., et al. 2011, ApJL, 726, L20

Origlia, L., Massari, D., Rich, R. M., et al. 2013, ApJL, 779, LL5

Origlia, L., Mucciarelli, A., Fiorentino, G., et al. 2019, ApJ, 871, 114

Ortolani, S., Bica, E., & Barbuy, B. 1996, A&A, 306, 134

Ortolani, S., Barbuy, B., Bica, E., et al. 2001, A&A, 376, 878

Pallanca, C., Dalessandro, E., Ferraro, F. R., et al. 2010, ApJ, 725, 1165

Pallanca, C., Dalessandro, E., Ferraro, F. R., Lanzoni, B., & Beccari, G. 2013, ApJ, 773, 122

Pallanca, C., Ransom, S. M., Ferraro, F. R., et al. 2014, ApJ, 795, 29

Pallanca, C., Beccari, G., Ferraro, F. R., et al. 2017, ApJ, 845, 4

Pallanca, C., Ferraro, F. R., Lanzoni, B., et al. 2019, ApJ, 882, 159

Pallanca, C., Lanzoni, B., Ferraro, F. R., et al. 2021, arXiv:2104.09362

Piotto, G., Zoccali, M., King, I. R., et al. 1999, AJ, 118, 1727

Popowski, P. 2000, ApJL, 528, L9

Rodrigo, C., Solano, E., & Bayo, A. 2012, IVOA Working Draft 15 October 2012. doi:10.5479/ADS/bib/2012ivoa.rept.1015R

Rodrigo, C. & Solano, E. 2020, Contributions to the XIV.0 Scientific Meeting (virtual) of the Spanish Astronomical Society, 182

Saha, A., Vivas, A. K., Olszewski, E. W., et al. 2019, ApJ, 874, 30. doi:10.3847/1538-4357/ab07ba

Saracino, S., Dalessandro, E., Ferraro, F. R., et al. 2015, ApJ, 806, 152

Saracino, S., Dalessandro, E., Ferraro, F. R., et al. 2019, ApJ, 874, 86

Schultz, G. V. & Wiemer, W. 1975, A&A, 43, 133

Stetson, P. B. 1987, PASP, 99, 191

Sneden, C., Gehrz, R. D., Hackwell, J. A., et al. 1978, ApJ, 223, 168.

Stetson, P. B. 1994, PASP, 106, 250

Tacchella, S., Lang, P., Carollo, C. M., et al. 2015, ApJ, 802, 101

Valenti, E., Ferraro, F. R., & Origlia, L. 2010, MNRAS, 402, 1729

von Braun, K., & Mateo, M. 2001, AJ, 121, 1522

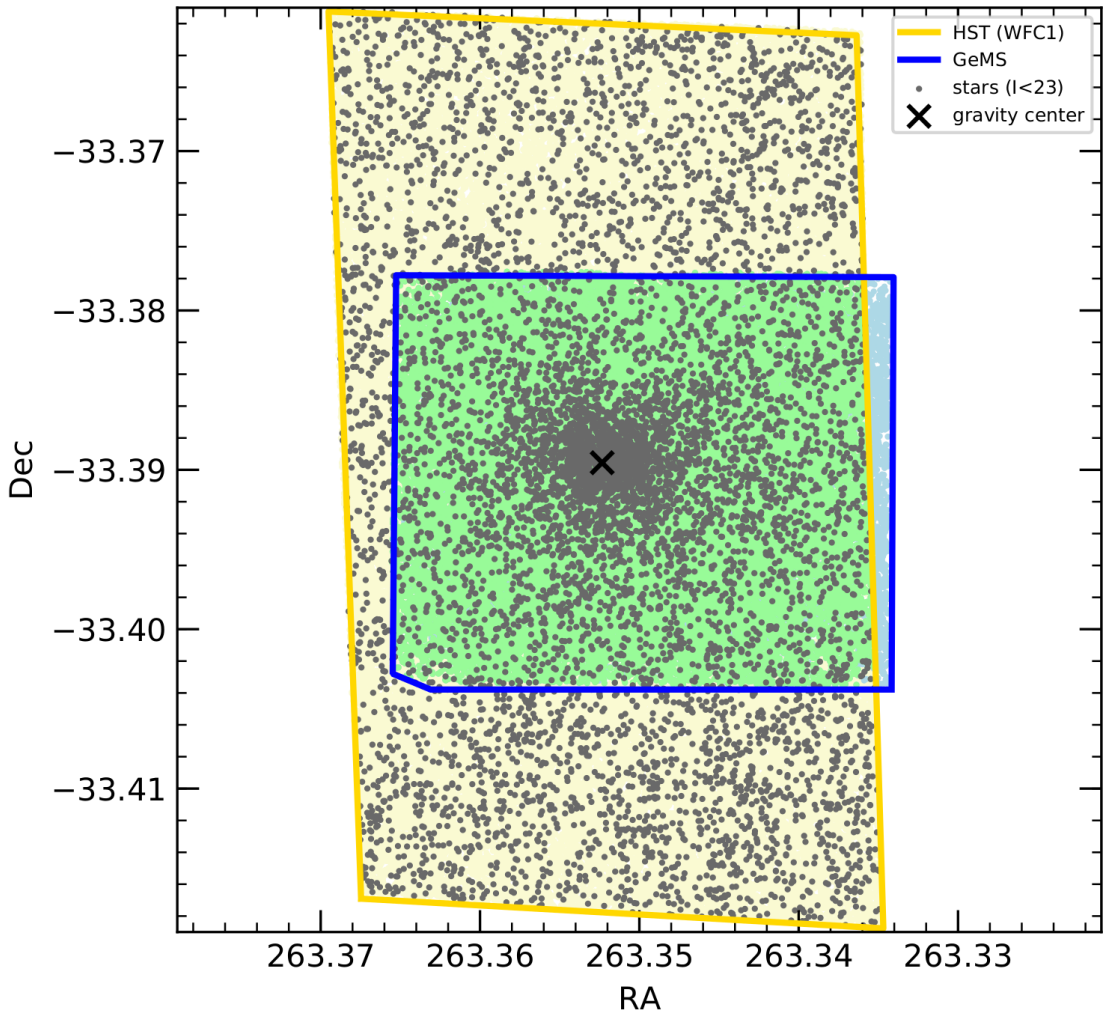

Figure 1. Field of view sampled by the observations: in yellow all the stars within the rectangular area of $\sim 200'' \times 100''$ covered by chip1 of the ACS-WFC data-set, outlined in blue the objects detected within the $\sim 100'' \times 90''$ region corresponding to the GeMS/GSAOI observations, and in green the stars detected in the field of view in common between the two data-sets, for which we determined the differential reddening map. For reference, we also show the position of all the detected stars with $I < 23$ (gray dots) and the gravity center (i.e. the photometric barycenter) of Liller 1 (black cross; Saracino et al. 2015).

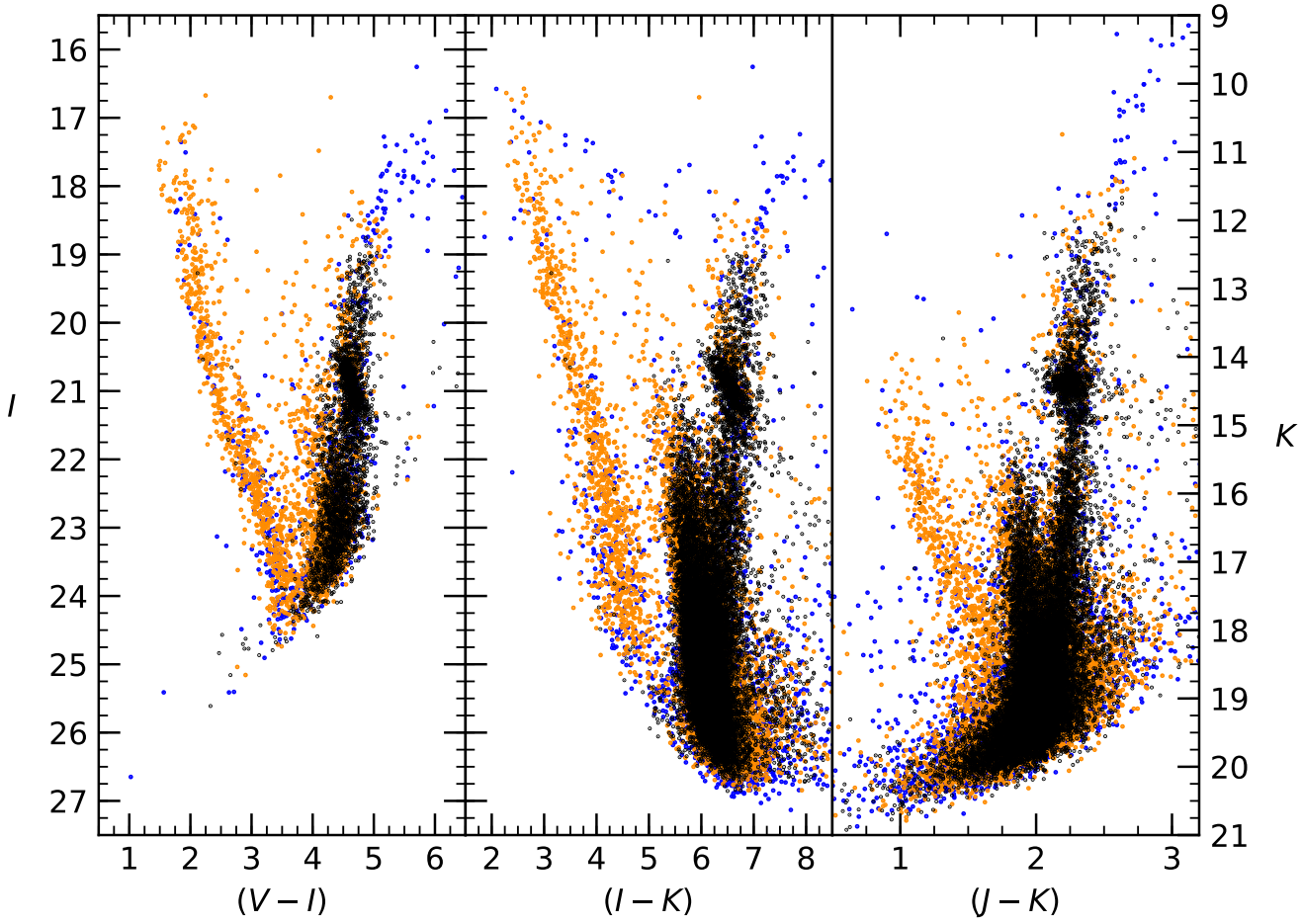

Figure 2. CMDs of Liller 1 obtained from the combination of optical HST data and GeMS NIR observations in the common field of view (the green area in Figure 1): from left to right, the purely optical $(I, V-I)$ CMD, the hybrid $(I, I-K)$ CMD, and the purely NIR $(K, J-K)$ diagram. Black and orange dots mark, respectively, the stars considered to be Liller 1 members and Galactic field interlopers, according to the proper motion analysis presented in Dalessandro E. et al. (2021; in preparation). The blue dots correspond to stars for which the proper motion measure is not available. The effect of differential reddening is well evident from the elongated morphology of the red clump, especially in the optical and hybrid CMDs.

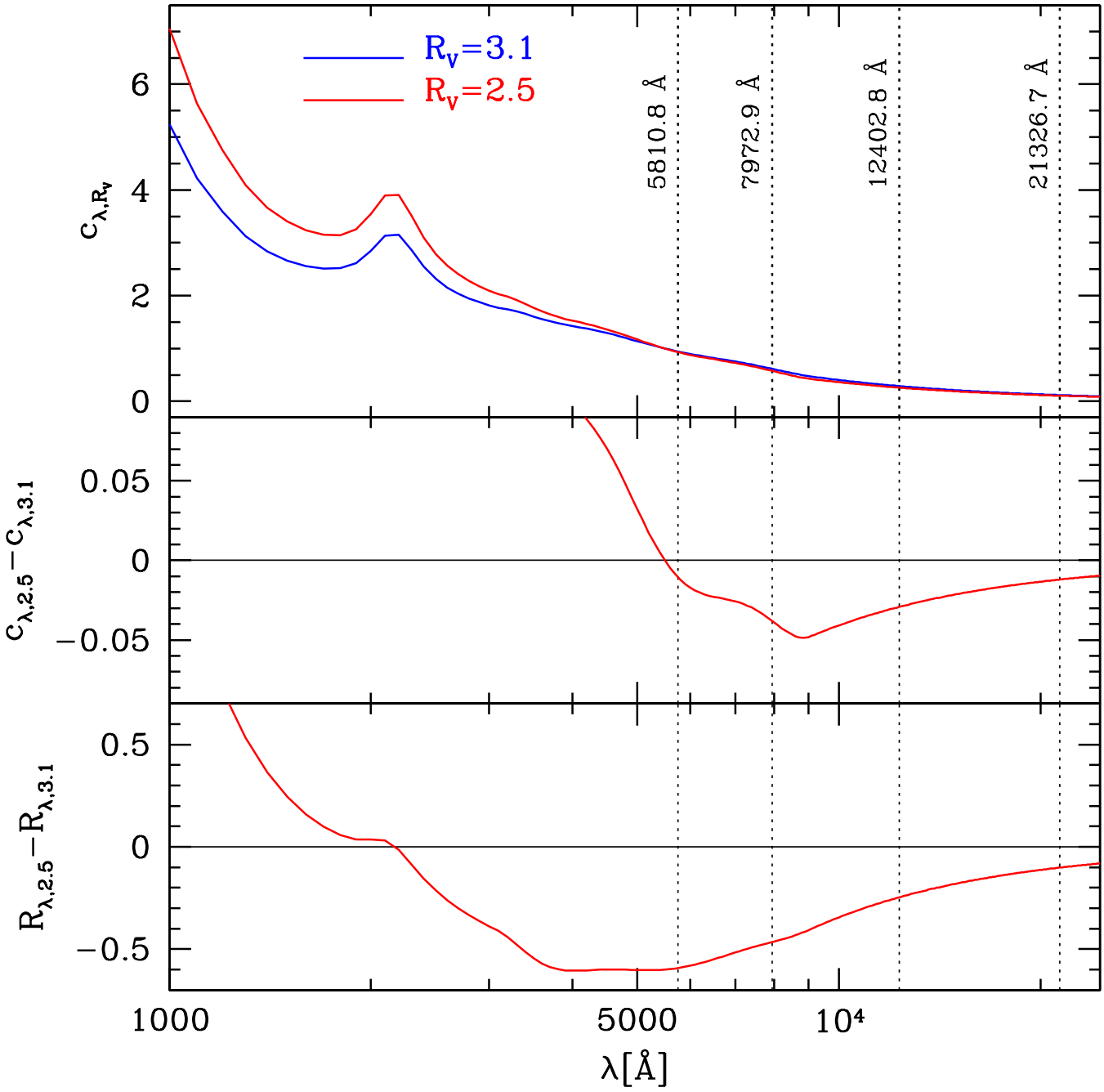

Figure 3. *Upper panel:* Dependence of the extinction law c_{λ,R_V} (or $\mathrm{A}_\lambda/\mathrm{A}_V$) on wavelength for two different assumptions of the R_V coefficient: the standard value for diffuse interstellar medium $\mathrm{R}_V = 3.1$ (blue line), and $\mathrm{R}_V = 2.5$ (red line). The vertical dotted lines are drawn in correspondence of the central wavelengths of the four photometric filters used in this work (see labels). *Middle panel:* Difference between $c_{\lambda,2.5}$ and $c_{\lambda,3.1}$ as a function of wavelength. *Lower panel:* Difference between $\mathrm{R}_{\lambda,2.5}$ and $\mathrm{R}_{\lambda,3.1}$ as a function of wavelength, with $\mathrm{R}_{\lambda,\mathrm{R}_V}$ defined as the product between R_V and c_{λ,R_V}, or the ratio between the absorption coefficient A_λ and the color excess $\mathrm{E}(B-V)$.

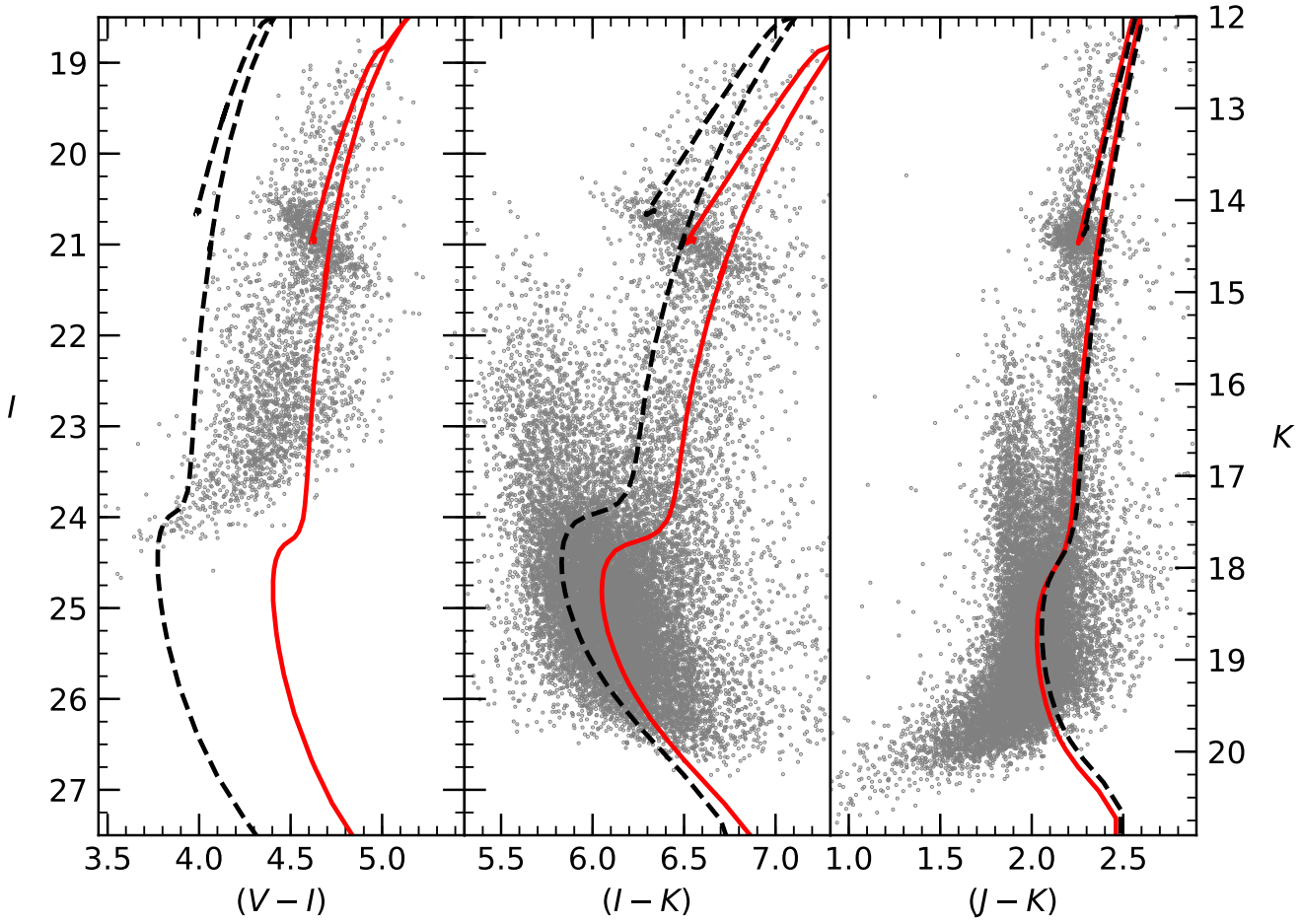

Figure 4. Optical, hybrid and NIR CMDs of Liller 1 obtained from well-measured and PM-selected member stars (grey dots), with a 12 Gyr old, [M/H]= −0.3 isochrone superposed. The black dashed line marks the position of the isochrone in the three CMDs obtained under the assumption of $R_V = 3.1$ by requiring that it well reproduces the NIR CMD: the corresponding values of mean absolute color excess and distance modulus are: $E(B-V) = 3.30$ and $\mu_0 = 14.55$ (Saracino et al. 2015). It is clearly unable to also match the hybrid and optical CMDs. The red solid line marks the position of the isochrone under the assumption of $R_V = 2.5$ and the request to well match the black dashed line in the NIR CMD, implying $E(B-V) = 4.52$ and $\mu_0 = 14.65$. As apparent, it well reproduces the observations in all the available color combinations.

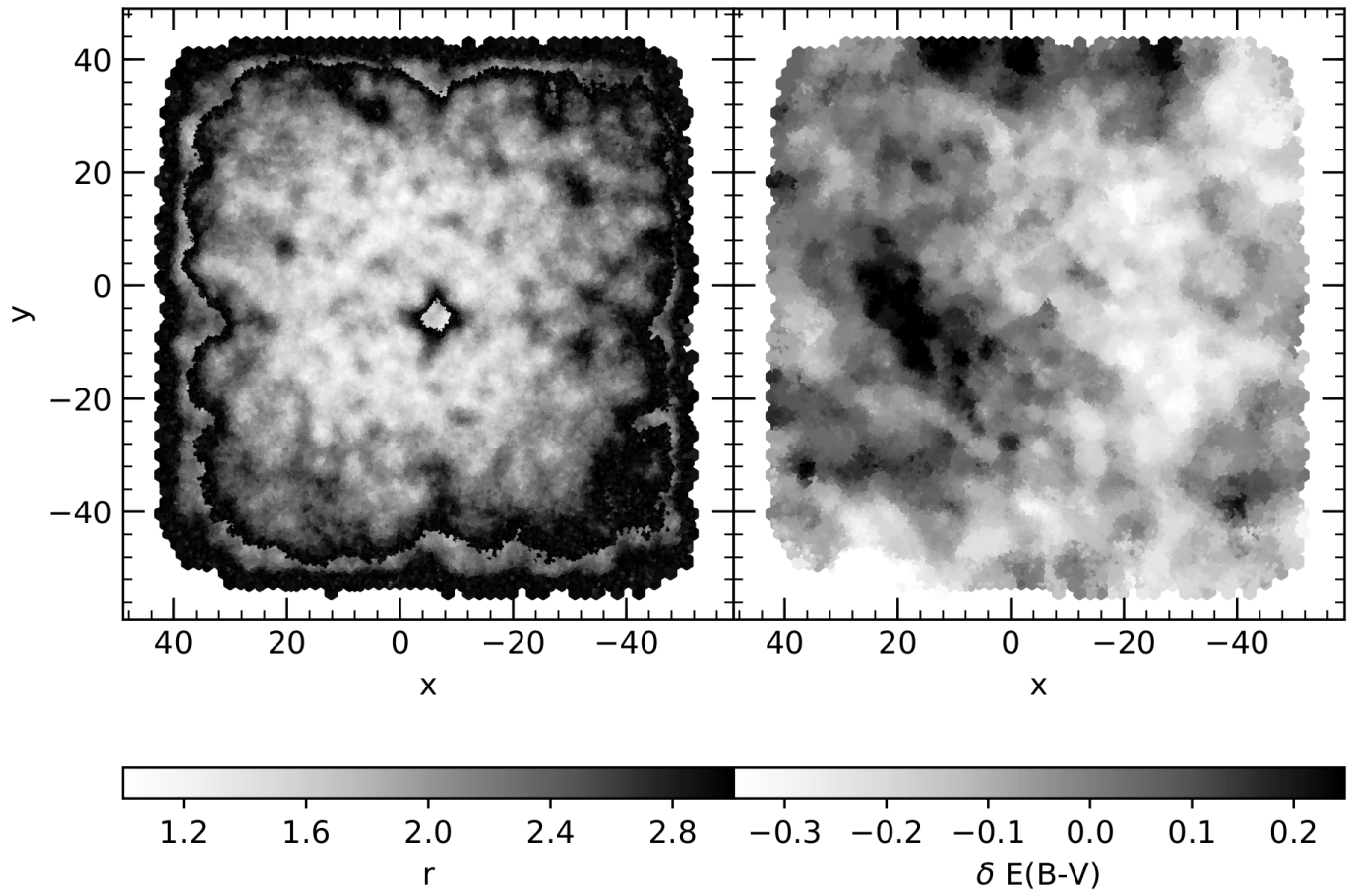

Figure 5. *Left panel:* Map of the radial distances (r, arcsec) used to select the samples of nearby sources for the construction of the "local CMD" of every star in the procedure adpoted to determine the differential reddening map. Lighter colors are associated to the best reached spatial resolution ($\sim 1''$), while darker colors correspond to the regions where $r_{\rm lim} = 3''$ is reached. The discontinuities in the r distribution are due to the two different catalogs (with and without the proper motion information) used to estimate the differential reddening. See Section 3.2 for more details. *Right panel:* Differential reddening map. The values of δE$(B-V)$ are both negative and positive since they are referred to the MRL of the OP. The associated colorbar codifies the δE$(B-V)$ values ranging from less extincted regions (lighter colors) to more extincted areas (darker colors).

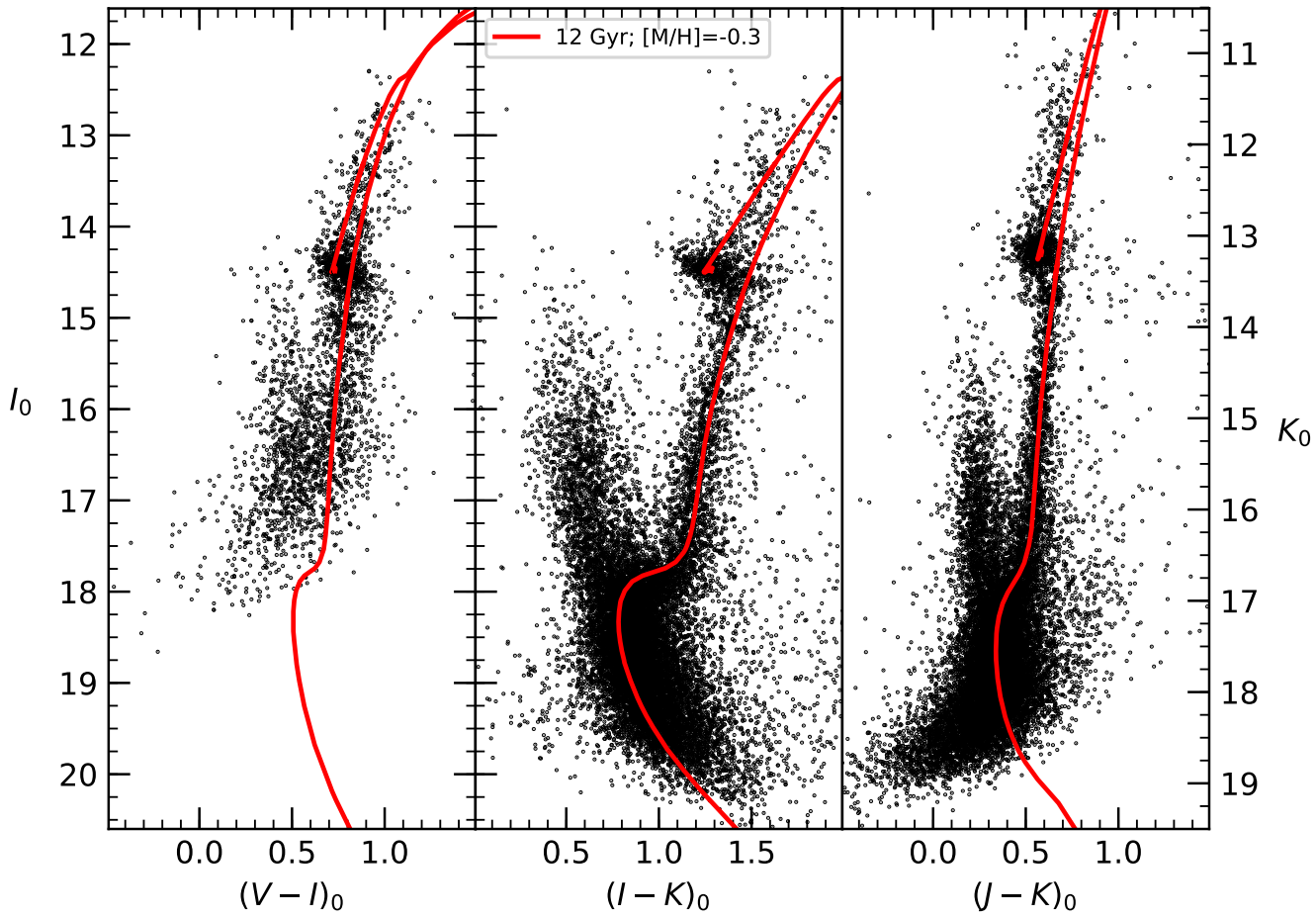

Figure 6. CMDs of of well-measured and PM-selected stars of Liller 1 after the correction for absolute differential reddening. A 12 Gyr old isochrone with a metallicity [M/H]= −0.3, obtained under the assumption of $R_V = 2.5$, $E(B-V) = 4.52$ and $\mu_0 = 14.65$ (same as the red lines in Figure 4) is also shown in all the panels.

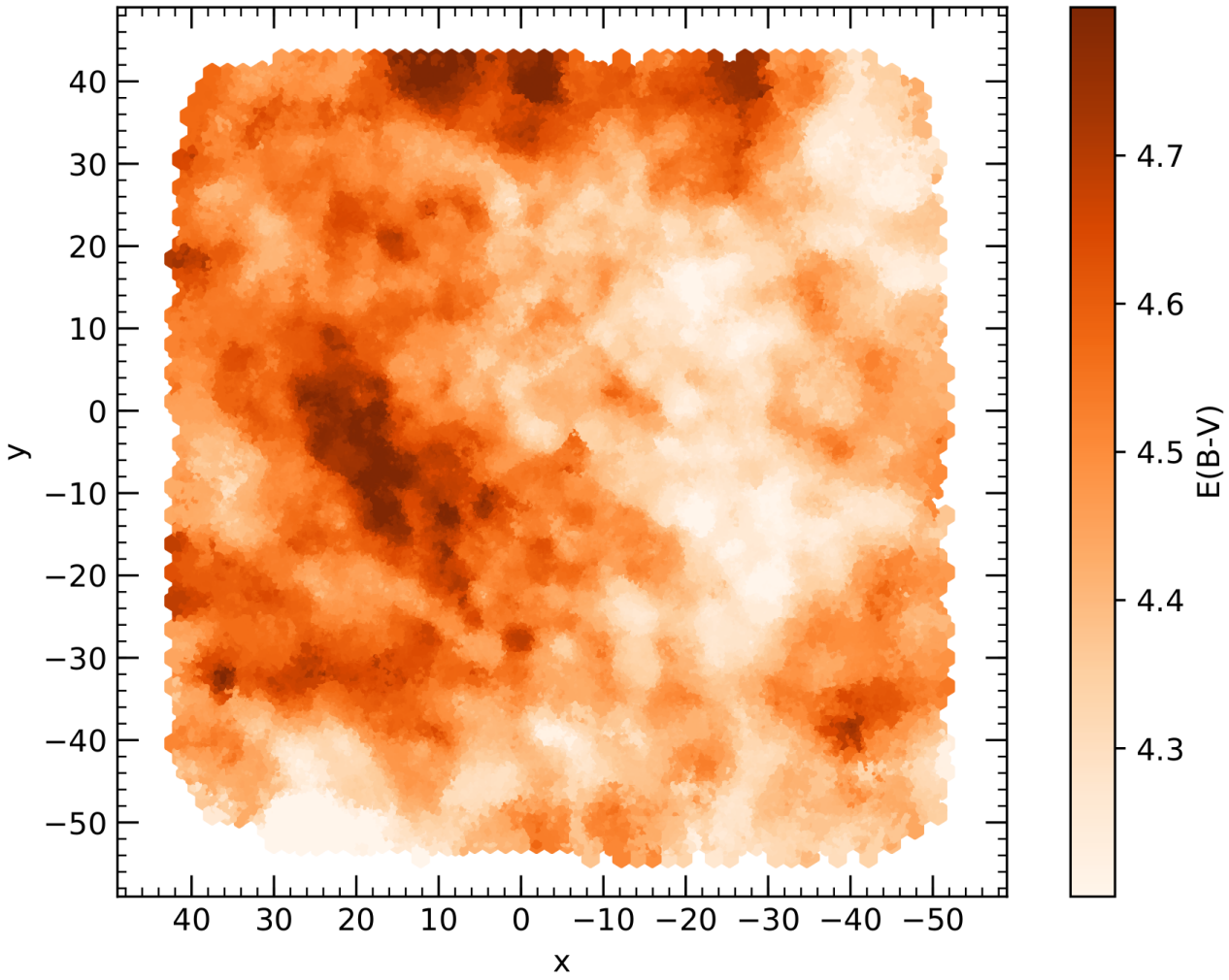

Figure 7. Absolute reddening map in the direction of Liller 1. The associated colorbar codifies the absolute values of E($B-V$), from less extincted regions (lighter colors), to more absorbed areas (darker colors).

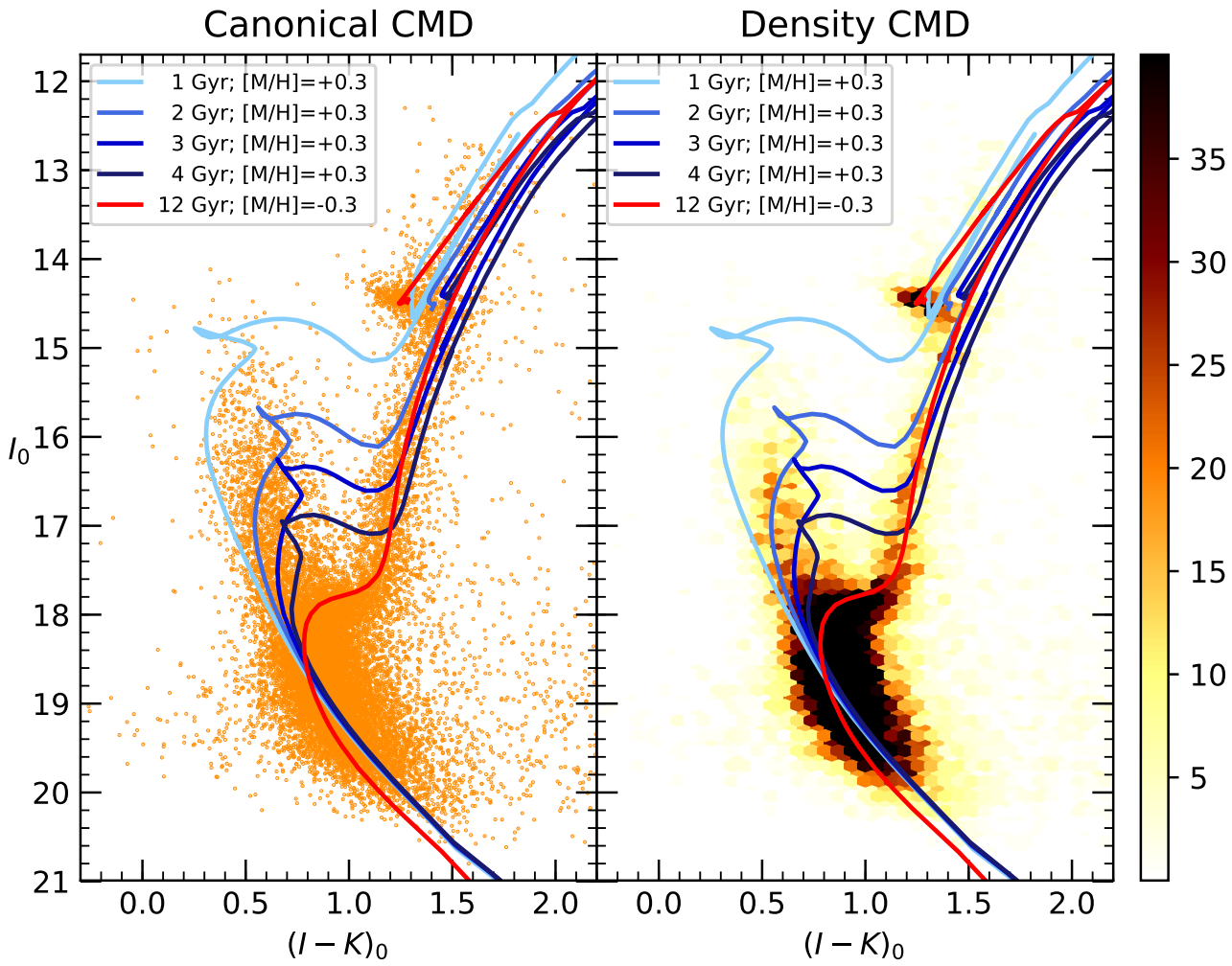

Figure 8. Differentially reddening corrected hybrid CMD with isochrones of different ages and metallicities (see labels) over-plotted. The left panel shows a canonical CMD (where every dot is a resolved star), while the right panel provides a density CMD (Hess diagram), where darker colors correspond to larger stellar densities in the CMD (see the color-bar on the right). Both visualisations highlight the clear presence of a 1-3 Gyr old stellar component, co-existing with an old (12 Gyr) and likely more metal-poor population.